Published in final edited form as:

Med Image Anal. 2023 July ; 87: 102812. doi:10.1016/j.media.2023.102812.

Learning pyramidal multi-scale harmonic wavelets for identifying the neuropathology propagation patterns of Alzheimer's disease

Huan Liu[a], **Hongmin Cai**[a], **Defu Yang**[b], **Wentao Zhu**[c], **Guorong Wu**[b], **Jiazhou Chen**[a,*]

[a]School of Computer Science and Engineering, South China University of Technology, Guangzhou, Guandong 510006, China

[b]Department of Psychiatry, University of North Carolina at Chapel Hill, Chapel Hill, NC 27599, USA

[c]Zhejiang Lab, Hangzhou, Zhejiang 311121, China

Abstract

Previous studies have established that neurodegenerative disease such as Alzheimer's disease (AD) is a disconnection syndrome, where the neuropathological burdens often propagate across the brain network to interfere with the structural and functional connections. In this context, identifying the propagation patterns of neuropathological burdens sheds new light on understanding the pathophysiological mechanism of AD progression. However, little attention has been paid to propagation pattern identification by fully considering the intrinsic properties of brain-network organization, which plays an important role in improving the interpretability of the identified propagation pathways. To this end, we propose a novel harmonic wavelet analysis approach to construct a set of region-specific pyramidal multi-scale harmonic wavelets, it allows us to characterize the propagation patterns of neuropathological burdens from multiple hierarchical modules across the brain network. Specifically, we first extract underlying hub nodes through a series of network centrality measurements on the common brain network reference generated from a population of minimum spanning tree (MST) brain networks. Then, we propose a manifold learning method to identify the region-specific pyramidal multi-scale harmonic wavelets corresponding to hub nodes by seamlessly integrating the hierarchically modular property of the brain network. We estimate the statistical power of our proposed harmonic wavelet analysis approach on synthetic data and large-scale neuroimaging data from ADNI. Compared with the other harmonic analysis techniques, our proposed method not only effectively predicts the early stage of AD but also provides a new window to capture the underlying hub nodes and the propagation pathways of neuropathological burdens in AD.

---

[*] Corresponding author. csjzchen@scut.edu.cn (J. Chen).

Declaration of competing interest

The authors declare that they have no known competing financial interests or personal relationships that could have appeared to influence the work reported in this paper.

Appendix A. Supplementary data

Supplementary material related to this article can be found online at https://doi.org/10.1016/j.media.2023.102812.

Keywords

Alzheimer’s disease; Brain network; Harmonic wavelets; Propagation pathway

MSC:

41A05; 41A10; 65D05; 65D17

1. Introduction

Alzheimer’s Disease (AD) is acknowledged as a progressive multifarious neurodegenerative disorder with the leading cause of memory loss, language impairment, disorientation, emotional instability, loss of motivation, and other behavioral problems when people are aging (Kumar et al., 2015; Mattson, 2004). Currently, the biological mechanisms underlying AD are not thoroughly understood, and no effective treatment exists (Stam, 2014). Therefore, accurate prediction of developing AD at its early stage becomes critical in slowing down the progression of AD via the appropriate interventions.

Recent developments in diffusion-weighted imaging (DWI) and network neuroscience allow us to characterize the white matter fiber bundles that connect various grey matter areas in the context of the large-scale brain network (Conturo et al., 1999). Moreover, convergent evidence shows that AD can be understood as a disconnection syndrome where neuropathological processes progressively disrupt the large-scale brain network (Pievani et al., 2014; Wu et al., 2016; Sepulcre et al., 2018). Such brain-network changes in AD are manifested much earlier before the onset of clinical symptoms (Araque Caballero et al., 2018; Filippi et al., 2017), indicating that accurately discovering the propagation pathways of neuropathological burdens provides a new window to predict the risk of developing AD at its early phase. In this regard, it is necessary to study the fundamental aspects of the brain-network organization, which can be used to promote the power in identifying the propagation patterns of neuropathological events and better understand the pathophysiological mechanism in AD.

Unlike many other real networks, the brain network generally exhibits properties of small-worldness and free scale, where the human brain is a hierarchical module organization, and hubs connect those modules. The high clustering of connections between nodes in the same module will favor locally segregated processing of specialized functions, while the short path length will support globally integrated processing of more generic functions (Sporns et al., 2004). Firstly, the hub nodes are usually located in the central positions of the network, exhibiting a much higher centrality than other nodes (van den Heuvel and Sporns, 2013), as shown in red and green nodes in Fig. 1(a). Based on the setting of network modules, hub nodes can be divided into two different categories, provincial hubs and connector hubs. Specifically, provincial hubs are the high-degree nodes that primarily connect to nodes in the same module (red nodes in Fig. 1(a)). Whereas, connector hubs are high-degree nodes that mainly connect to several different modules in the brain network (green nodes in Fig. 1(a)). In addition, emerging evidence shows that neuropathological disruption selectively accumulates at some critical hub regions (Cope et al., 2018; Dai et al., 2015; Wang et al., 2020; Li et al., 2022). Secondly, hierarchical modularity is a type of network organization where each module in the brain network can be further partitioned into a set of sub-modules, and within each sub-module there may be sub-sub-modules (shown in Fig. 1(b)). And the hierarchical modularity gives the brain network the advantage of greater robustness, adaptivity, and evolvability of network function. Therefore, considering the hierarchical characteristic of the brain network in the developed methods would enhance the performance in identifying the brain-network changes in AD (Huang et al., 2021).

Recently, mounting evidence shows the whole brain network can be summarized as its own Eigensystem, which is a set of harmonic waves derived from the underlying Laplacian matrix of the brain network (Atasoy et al., 2016, 2017). Some studies have extended the discovery to Alzheimer's disease, Chen et al. (2020b,a) first proposed a manifold learning approach to identify the global common harmonic waves from a set of brain networks, which can be used to characterize the network alterations in the graph spectrum domain. This method offers a new window into the investigation of frequency-based alterations in AD progression. Moreover, Chen et al. (2021) extended global common harmonic waves to localized harmonic wavelets by developing a harmonic localization method. This method generates a set of local single-scale harmonic wavelets (shown in Fig. 1(c)) where the oscillation patterns in each harmonic wavelet characterize the spreading pathway that can be used to investigate the local propagation patterns of neuropathology within a single hierarchical module. These methods demonstrate the ability of the harmonic analysis approach as a new brain network analysis technique to discover the propagation pathway of neuropathological burdens, which is more attractive in AD studies. However, the current harmonic wavelet identification approaches lack adequate consideration of the intrinsic properties of brain-network organization, limiting their performance in characterizing the accurate and interpretable propagation patterns of neuropathological events in the brain.

To overcome this limitation, we propose a novel harmonic wavelet analysis approach, which seamlessly incorporates topological characteristics in complex brain networks to discover a set of region-specific pyramidal multi-scale harmonic wavelets in the spatial domain of brain. Such learned harmonic wavelets allow us to characterize the propagation patterns of neuropathological burdens from multiple hierarchical modules across the brain network. Specifically, we first select the nodes with high centrality as the underlying hub nodes via a broad array of network centrality measures, including node degree, betweenness, pagerank, and participation coefficient, as shown in Fig. 2(a). Then, we design a hierarchically modular binary mask representation method to effectively describe the hierarchically modular property of the brain network (Fig. 2(b)). Next, a set of region-specific pyramidal multi-scale harmonic wavelets (Fig. 2(c)) in the spatial domain of a hierarchical module (Fig. 2(b)) can be obtained via our proposed method. Since the spreading of the neuropathological burdens follows the topology of the brain network (Fig. 2(d)), a new imaging biomarker depicting the resonance between the spatial pattern of pathological burdens and the oscillation pattern in the harmonic wavelet can be used to identify the AD-related spreading pathways of neuropathological events throughout the brain (Fig. 2(e)).

We have evaluated the statistical power of our method on synthetic data and neuroimaging data from the ADNI database. Compared with other state-of-the-art harmonic analysis approaches, our proposed method achieves higher performance for classifying CN (cognitively normal), EMCI (early-stage mild cognitive impairment), and LMCI (late-state mild cognitive impairment) comparison. Furthermore, we have not only identified a set of brain regions that can be used as potential hub nodes leading to cognitive decline in AD progression, but also discovered the AD-related propagation patterns of neuropathological burdens spreading across brain networks.

2. Method

In this section, we first introduce the brief background on MST brain network and harmonic waves on brain network in Section 2.1. We then construct a harmonic wavelet analysis framework to identify a set of region-specific pyramidal multi-scale harmonic wavelets across the brain network in Section 2.2, followed by the optimization scheme in Section 2.3. The application of the learned multi-scale harmonic wavelets is demonstrated in Section 2.4. The notation used in this paper is summarized in Table 1 for ease of exposition.

2.1. Background: MST brain network and harmonic waves on brain network

2.1.1. MST brain network—In graph theory, each brain network constructed through MRI and DTI neuroimages can be represented as a graph $G = (V, E, \boldsymbol{W})$, with node set $V = \{v_i \mid i \in 1, \ldots, N\}$ from N brain regions and edge set $E = \{e_{ij} \mid (v_i, v_j) \in V \times V\}$ representing all possible links between nodes. The symmetric adjacency matrix $\boldsymbol{W} = [w_{ij}]_{N \times N} \in \mathbb{R}^{N \times N}$ with non-negative weights w_{ij} reflects the strength of node–node connection.

Reconstructing the MST brain network $\widetilde{\boldsymbol{W}}$ based on the adjacency matrix $\boldsymbol{W}$ is a valid way to describe the brain network topology unbiased (van Dellen et al., 2018). In our method, the MST brain network is constructed by Kruskal's algorithm (Kruskal, 1956), which is realized by following steps: (1) Rank all edges in descending order; (2) Select edge with maximum weight unless the edge makes those nodes into a loop; (3) Repeat step 2 until all nodes are in the tree.

2.1.2. Harmonic waves on brain network—As stated in Atasoy et al. (2016), we derive a set of harmonic waves $\boldsymbol{\Psi} \in \mathbb{R}^{N \times P}$ from the eigen-system of the underlying Laplacian matrix $\boldsymbol{L} = \boldsymbol{D} - \boldsymbol{W}$, where the diagonal matrix $\boldsymbol{D}(i, i) = \sum_{j=1}^{N} w_{ij}$ can be regarded as the degree matrix of the graph. Each diagonal element indicates the total connectivity degree of the underlying node. Specifically, the harmonic waves $\boldsymbol{\Psi}$ are estimated by solving the following eigenvalue problem:

$$\min_{\Psi \in \mathbb{R}^{N \times P}} Tr\left(\Psi^T L\, \Psi\right) \ s.t.\ \Psi^T \Psi = I_P \tag{1}$$

where $Tr(\cdot)$ is the trace operator and $\boldsymbol{I}_P$ denotes the $P \times P$ identity matrix. The deterministic solution $\boldsymbol{\Psi} = [\psi_p]_{p=1}^{P}$ consists of the eigenvectors of the Laplacian matrix $\boldsymbol{L}$ associated with the first P smallest eigenvalues $\{\lambda_p \mid p = 1, \ldots, P, \lambda_1 \leq \lambda_2 \leq \cdots \leq \lambda_P\}$, indicating the harmonic wave exhibits faster oscillation patterns across the brain network as the eigenvalue increases. Since the harmonic waves associated with the high frequency (larger eigenvalues) are often sensitive to possible noise, we only consider the first $P(P < N)$ harmonic waves.

2.2. Framework: Region-specific pyramidal multi-scale harmonic wavelet construction on stiefel manifold

2.2.1. Extraction of brain regions with high centrality—Suppose we have a set of MST brain networks $\left\{\widetilde{\boldsymbol{W}}_t \mid t = 1, \ldots, T\right\}$, we can calculate the group-mean adjacency matrix $\bar{\boldsymbol{W}}$ by averaging all MST brain networks $\left\{\widetilde{\boldsymbol{W}}_t\right\}$, i.e., $\bar{\boldsymbol{W}} = \frac{1}{T}\sum_{t=1}^{T} \widetilde{\boldsymbol{W}}_t$. In network neuroscience, the brain network is usually composed of many peripheral regions and some central regions, i.e., hubs, which manifest the key roles in transmitting and communicating hierarchical information (Li et al., 2022). As introduced in van den Heuvel and Sporns (2013), several network nodal measurements can be used to extract the brain regions with high centrality. For instance, the degree centrality is measured as the number of edges on nodes, and it is an appropriate measurement for identifying hub nodes. The pagerank centrality tends to detect nodes connected to other highly central nodes, and the betweenness centrality is defined as the number of shortest communication paths in the network that pass through a given node. The participation coefficient measures the distribution of the node's edges, which achieves by maximizing the number of within-group edges and minimizing the number of between-group edges, so it is closely connected with provincial hubs and connector hubs. To this end, we select nodes with high centrality as underlying hub nodes by calculating a composite score of node degree, betweenness, pagerank, and participation coefficient on $\bar{\boldsymbol{W}}$. Specifically, we first calculate the scores of degree, betweenness, pagerank, and participation coefficient at each node separately, where the computational details of these four centrality measurements are shown in Suppl. Tab. S1. Then, we normalize those scores of all nodes to the range of 0 to 1. Next, we sort all nodes according to the final composite score obtained by combining these four normalized centrality measurements in descending order. Lastly, we select top m nodes $\{v_i \mid i = 1, \ldots, m\}$ as the underlying hub nodes by a given threshold. In our experiments on the ADNI database, the 40 nodes with the highest composite score (blue nodes) are designated as underlying hub nodes, as shown in Fig. 3.

2.2.2. Construction of region-specific pyramidal multi-scale harmonic wavelets—Given the group-mean adjacency matrix $\bar{\boldsymbol{W}}$, the common harmonic waves $\boldsymbol{\Psi}$ can be calculated by Eq. (1). Since the $N \times P$ orthogonal matrix $\boldsymbol{\Psi}$ located on the Stiefel manifold (Chikuse, 2003), it is suitable to be used as a common brain network harmonic bases (Atasoy et al., 2016, 2017) to characterize the frequency-based energy representations of each instance of neuropathological burdens $f = [f_j]_{j=1}^{N}$ propagating throughout the brain network. However, the common harmonic waves have the limitation of global nature, like the Fourier bases in signal processing. In practical neuroscience applications, the spreading pathway of neuropathological events exhibits more localized propagation patterns that occur in hierarchical modules at particular brain regions (Vogel et al., 2020). To address this drawback, we provide region-specific pyramidal multi-scale complementary to the global harmonics by integrating the region-specific and hierarchically modular constraints to Eq. (1).

In this section, we present the following three components to learn the region-specific pyramidal multi-scale harmonic wavelets $\boldsymbol{\Phi}_{i,k} = [\varphi_{i,k,q}]_{q=1}^{Q} \in \mathbb{R}^{N \times Q}$ on kth hierarchical module at the underlying hub node v_i, where the Q stands for the number of wavelet frequencies.

First, the region-specific pyramidal multi-scale harmonic wavelets $\boldsymbol{\Phi}_{i,k}$ is required to preserve the localized topological structure of brain network. Thus, this can be obtained by minimizing a harmonic energy term $E_{smooth}(\boldsymbol{\Phi}_{i,k}) = Tr(\boldsymbol{\Phi}_{i,k}^T \bar{\boldsymbol{L}} \boldsymbol{\Phi}_{i,k})$. In addition, we constrain $\boldsymbol{\Phi}_{i,k}$ to be an orthogonal base resided on the Stiefel manifold, i.e. $\boldsymbol{\Phi}_{i,k}^T \boldsymbol{\Phi}_{i,k} = \boldsymbol{I}_Q$.

Second, to reflect the hierarchically modular property of the brain network, we define a set of hierarchical modules on each underlying hub node v_i in the network $\boldsymbol{G}$, $\boldsymbol{G}_{i,h} = \{\boldsymbol{G}_{i,k} = (V_{i,k}, E_{i,k})\}_{k=1,2,\ldots,h}$, where $V_{i,k} = \{v \in V \mid s(v, v_i) \leq k\}$, $E_{i,k} = \{(v', v) \in E \mid v', v \in V_{i,k}\}$, and $s(\cdot, v_i)$ is the length of the shortest-path between node v_i and the other node based on group-mean adjacency matrix $\bar{\boldsymbol{W}}$. Here, parameter h stands for the number of hierarchical modules in the set $\boldsymbol{G}_{i,h}$. In our real experiments, we set $h = 3$ according to the density of the brain network. Furthermore, to integrate the hierarchical modularity of brain network into each harmonic wavelets $\boldsymbol{\Phi}_{i,k}$, we require that the support of $\boldsymbol{\Phi}_{i,k}$ does not expand more than kth hierarchical module centered at the underlying hub node v_i, i.e., $\boldsymbol{G}_{i,k}$. To achieve this goal, we introduce a hierarchically modular binary mask $\boldsymbol{u}_{i,k} = [u_{i,k}(j)]_{j=1}^{N}$ as an auxiliary vector:

$$\boldsymbol{u}_{i,k}(j) = \begin{cases} 1 & v_j \in V_{i,k} \text{ in the hierarchical module } \boldsymbol{G}_{i,k}, \\ 0 & \text{otherwise.} \end{cases}$$

Finally, a region-specific pyramidal multi-scale harmonic wavelet presentation term can be defined by $E_{local}(\boldsymbol{\Phi}_{i,k}) = Tr\left(\boldsymbol{\Phi}_{i,k}^T diag(1 - \boldsymbol{u}_{i,k}) \boldsymbol{\Phi}_{i,k}\right)$, where $diag(\cdot)$ denotes the vector diagonalization. Minimizing $E_{local}(\boldsymbol{\Phi}_{i,k})$ tends to optimize $\| \boldsymbol{\Phi}_{i,k} \|^2$ to be zero out of the hierarchical module $\boldsymbol{G}_{i,k}$. Since $diag(1 - \boldsymbol{u}_{i,k})$ is zero for the nodes in $\boldsymbol{G}_{i,k}$ and has no effect in minimizing the energy term E_{local}, it can be used to suppress the waves (oscillations) out of $\boldsymbol{G}_{i,k}$ while preserving the waves in $\boldsymbol{G}_{i,k}$.

Third, to reduce the redundancy between global common harmonic waves $\boldsymbol{\Psi}$ and each harmonic wavelets $\boldsymbol{\Phi}_{i,k}$ at node v_i, we require common harmonics $\boldsymbol{\Psi}$ to be independent of each harmonic wavelets $\boldsymbol{\Phi}_{i,k}$ via constraint $\boldsymbol{\Phi}_{i,k}^T \boldsymbol{\Psi} = 0$. To facilitate the computational complexity, we relax the constraint alternatively by promoting the orthogonality to the subspace spanned by $\boldsymbol{\Psi}$, through minimizing $E_{orth}(\boldsymbol{\Phi}_{i,k}) = Tr(\boldsymbol{\Phi}_{i,k}^T \boldsymbol{\Psi} \boldsymbol{\Psi}^T \boldsymbol{\Phi}_{i,k})$. Similarly, we require that harmonic wavelets with different scales are orthogonal to each other, i.e. $\boldsymbol{\Phi}_{i,k}^T \boldsymbol{\Phi}_{i,l} = 0_Q, \forall k, l \in \{1,2,3\}, k \neq l$.

Finally, the whole energy function of identifying region-specific pyramidal multi-scale harmonic wavelets $\boldsymbol{\Phi}_{i,k}$ in kth hierarchical module centered at the underlying hub node v_i is formulated as:

$$\min_{\{\boldsymbol{\Phi}_{i,k}\}} \sum_{k=1}^{3} \left\{ Tr\left(\boldsymbol{\Phi}_{i,k}^{T} \bar{L} \boldsymbol{\Phi}_{i,k}\right) \right.$$

$$\left. + \mu_1 Tr\left(\boldsymbol{\Phi}_{i,k}^{T} diag(1 - u_{i,k}) \boldsymbol{\Phi}_{i,k}\right) + \mu_2 Tr\left(\boldsymbol{\Phi}_{i,k}^{T} \Psi \Psi^{T} \boldsymbol{\Phi}_{i,k}\right) \right\} \tag{2}$$

$$s.t.\ \boldsymbol{\Phi}_{i,k}^{T} \boldsymbol{\Phi}_{i,k} = I, \boldsymbol{\Phi}_{i,k}^{T} \boldsymbol{\Phi}_{i,l} = 0, \forall k, l \in \{1, 2, 3\}, k \neq l$$

where μ_1 and μ_2 are two scalars balancing the strength of hierarchical modularity and redundancy with the global common harmonic waves $\boldsymbol{\Psi}$.

2.3. Optimization: Identify region-specific pyramidal multi-scale harmonic wavelets via manifold optimization

In this section, for each underlying hub node v_i, we first introduce a variable $\boldsymbol{\Omega}_i$, which is achieved by simply integrating $\boldsymbol{\Phi}_{i,1}$, $\boldsymbol{\Phi}_{i,2}$, $\boldsymbol{\Phi}_{i,3}$ into a new matrix $\boldsymbol{\Omega}_i = (\boldsymbol{\Phi}_{i,1}, \boldsymbol{\Phi}_{i,2}, \boldsymbol{\Phi}_{i,3}) \in \mathbb{R}^{N \times 3Q}$. Thus, the objective function in Eq. (2) can be rewritten as the following energy function form by simple mathematical transformations:

$$\min_{\Omega_i} Tr\left(\Omega_i^{T} \left(\bar{L} + \mu_2 \Psi \Psi^{T}\right) \Omega_i\right)$$

$$+ \mu_1 \sum_{k=1}^{3} \left\{ Tr\left(\Delta_k \Omega_i^{T} diag(1 - u_{i,k}) \Omega_i\right) \right\} \tag{3}$$

$$s.t.\ \Omega_i^{T} \Omega_i = I_{3Q}$$

where

$$\Delta_1 = \begin{pmatrix} I_Q & 0 & 0 \\ 0 & 0Q & 0 \\ 0 & 0 & 0_Q \end{pmatrix}, \Delta_2 = \begin{pmatrix} 0_Q & 0 & 0 \\ 0 & I_Q & 0 \\ 0 & 0 & 0_Q \end{pmatrix}, \Delta_3 = \begin{pmatrix} 0_Q & 0 & 0 \\ 0 & 0_Q & 0 \\ 0 & 0 & I_Q \end{pmatrix}$$

Since Eq. (3) is a typical quadratic problem on the Stiefel manifold, it often required that $\boldsymbol{A}_i = \bar{\boldsymbol{L}} + \mu_2 \boldsymbol{\Psi} \boldsymbol{\Psi}^{T} + \mu_1 \sum_{k=1}^{3} diag(1 - \boldsymbol{u}_{i,k})$ is positive definite. In order to achieve this, we introduce a relaxation parameter α, which makes sure $\widetilde{\boldsymbol{A}}_i = \alpha \boldsymbol{I} - \boldsymbol{A}_i$ is a positive definite matrix. α is set as the greatest eigenvalue of matrix $\boldsymbol{A}_i$. To simplify the formula, we use $\boldsymbol{B}_{i,k}$ to replace $diag(1 - \boldsymbol{u}_{i,k})$. By doing so, the minimization of Eq. (3) turns into maximizing:

$$\max_{\Omega_i} Tr\left(\Omega_i^{T} \left((\widetilde{A}_i + \mu_1 \sum_{k=1}^{3} B_{i,k}) \Omega_i - \mu_1 \sum_{k=1}^{3} B_{i,k} \Omega_i \Delta_k\right)\right) \tag{4}$$

$$s.t.\ \Omega_i^{T} \Omega_i = I_{3Q}$$

Furthermore, it can be rewritten as:

$$\max_{\Omega_i} \; Tr\left(\Omega_i^T M_i\right) \; s.t. \; \Omega_i^T \Omega_i = I_{3Q} \tag{5}$$

where

$$M_i = (\tilde{A}_i + \mu_1 \sum_{k=1}^{3} B_{i,k})\Omega_i - \mu_1 \sum_{k=1}^{3} B_{i,k}\Omega_i \Delta_k \tag{6}$$

It is apparent that the objective function in Eq. (5) can be simply solved by power iteration (Nie et al., 2017) in the following four steps:

1. Randomly initialize $\boldsymbol{\Omega}_i \in \mathbb{R}^{N \times 3Q}$ such that $\boldsymbol{\Omega}_i^T \boldsymbol{\Omega}_i = \boldsymbol{I}_{3Q \times 3Q}$ and α is the greatest eigenvalue after applying SVD to matrix $\boldsymbol{A}_i$.
2. Update $\boldsymbol{M}_i$ by calculating $(\tilde{\boldsymbol{A}}_i + \mu_1 \sum_{k=1}^{3} \boldsymbol{B}_{i,k})\boldsymbol{\Omega}_i - \mu_1 \sum_{k=1}^{3} \boldsymbol{B}_{i,k}\boldsymbol{\Omega}_i \Delta_k$.
3. Calculate $\boldsymbol{\Omega}_i$ by maximizing $Tr\left(\boldsymbol{\Omega}_i^T \boldsymbol{M}_i\right)$ and subject it to orthogonal constraint $\boldsymbol{\Omega}_i^T \boldsymbol{\Omega}_i = \boldsymbol{I}_{3Q}$. We can derive the closed-form solution by $\boldsymbol{\Omega}_i = \boldsymbol{U}\boldsymbol{V}^T$, where $\boldsymbol{U}$ and $\boldsymbol{V}$ are the left and right Eigen matrix after the SVD on $\boldsymbol{M}_i$.
4. Iteratively perform the step (2)~(3) until the algorithm converges.

Algorithm 1

Algorithm for Identifying Region-specific Pyramidal Multi-scale Harmonic Wavelets

```
Input: Parameters: $\mu_1, \mu_2$;
    Symmetry Graph Laplacian matrix $\bar{\boldsymbol{L}}$ of group-mean adjacency matrix $\bar{\boldsymbol{W}}$;
    Global common harmonic waves $\boldsymbol{\Psi}$ by calculating eigenvectors of $\bar{\boldsymbol{L}}$;
    Hierarchically modular binary mask $\boldsymbol{u}_{i,k}$ of k$^{th}$ layer at underlying hub node $\upsilon_i$;
    Randomly initialized orthogonal matrix $\boldsymbol{\Omega}_i \in \mathbb{R}^{N \times 3Q}$;
Output: $\{\boldsymbol{\Omega}_i \mid i = 1, \cdots, m\}$
for $i = 1,2, \cdots, m$ do
  while $\varepsilon > 0.01$ do
    Update $\boldsymbol{M}_i = (\tilde{\boldsymbol{A}}_i + \mu_1 \sum_{k=1}^{3} \boldsymbol{B}_{i,k})\boldsymbol{\Omega}_i - \mu_1 \sum_{k=1}^{3} \boldsymbol{B}_{i,k}\boldsymbol{\Omega}_i \Delta_k$
    Run the compact SVD method: $\boldsymbol{U}\boldsymbol{S}\boldsymbol{V}^T = \boldsymbol{M}_i$
    Update $\boldsymbol{\Omega}_i = \boldsymbol{U}\boldsymbol{V}^T$.
    Update $New_{cost} = Tr\left(\boldsymbol{\Omega}_i^T \boldsymbol{M}_i\right)$
    Update $\varepsilon = abs(New_{cost} - Old_{cost})$
    Update $Old_{cost} = New_{cost}$
  end while
end for
```

Consequently, the entire optimization scheme of identifying region-specific pyramidal multi-scale harmonic wavelets is summarized in Algorithm 1.

Hyperparameter Tuning.—In the proposed objective function in Eq. (2), we need to tune two types of parameters: harmonic number (P and Q) and hyperparameters (μ_1 and μ_2). Since the higher frequency harmonic waves tend to be sensitive to potential noise, we determine to use only the smallest P eigenvectors $\boldsymbol{\Phi}_s^P$ instead of the whole eigenvectors $\boldsymbol{\Phi}_s$. According to the reconstruction loss calculated by matrix norm between original Laplacian matrix $\boldsymbol{L}_s$ and the reconstructed Laplacian matrix $\hat{\boldsymbol{L}}_s^P = \left(\boldsymbol{\Phi}_s^P\right)^T \boldsymbol{\Lambda}^P \boldsymbol{\Phi}_s^P$ with $\boldsymbol{\Lambda}^P$ as the diagonal matrix of the first P eigen-value of the Laplacian matrix $\boldsymbol{L}_s$, the dimension P is determined, which is located at the stable point such that the reduction in reconstruction loss is marginal as P increases. Additionally, the number Q of harmonic wavelets $\boldsymbol{\Phi}_{i,k}$ is determined according to the average node degree of all underlying hub nodes. For the hyperparameter selection, we apply a grid search scheme to select the optimal parameters μ_1 and μ_2 based on the classification accuracy. In the following experiments on ADNI neuroimaging data, we set the harmonic number $P = 55$ and $Q = 6$, respectively. Regarding hyperparameters, we set $\mu_1 = 0.8$ and $\mu_2 = 0.7$ as the optimal parameters, achieving the best classification performance.

Computational Complexity and Convergence Analysis.—The complexity of Algorithm 1 is mainly dependent on SVD decomposition and matrix multiplication. In SVD decomposition, U and V are $(N \times 3Q)$ and $(3Q \times 3Q)$ matrices, so constructing these matrices has a time complexity of $O\left(NQ^2\right)$. While matrix multiplication has the same time complexity as SVD decomposition. In the whole algorithm, the maximal iteration number is H, and the number of samples is m; therefore, optimizing Algorithm 1 has the time complexity of $O\left(mHNQ^2\right)$. As shown in Algorithm 1, we adopt the generalized power iteration (GPI) to solve Eq. (5) on the Stiefel manifold. The convergence of the GPI algorithm has been theoretically proved by the theorem 1–2 in Nie et al. (2017).

2.4. Application: A new neuroimaging biomarker in AD

The empirical biomarkers such as amyloid deposition and tau tangle aggregation are the hallmarks of AD progression, which may be sufficient to cause downstream pathologic changes leading to cognitive decline (Jack Jr. et al., 2018). Traditional neuroimaging studies usually adopt empirical biomarkers to investigate the neuropathological mechanism of AD. In this work, we develop a novel harmonic wavelet analysis approach to discover the brain network changes that are associated with local propagation patterns of pathological burdens in multiple hierarchical modules at particular underlying hub nodes across the brain network. The learned region-specific pyramidal multi-scale harmonic wavelets $\{\boldsymbol{\Phi}_{i,k}\}$ are used to generate the new hierarchical-adaptive-wavelet representations (HAW in short) for each individual subject of observed empirical biomarkers $\boldsymbol{f} \in \mathbb{R}^N$ by:

$$\hat{\boldsymbol{h}}_{i,k,p} = |\langle \boldsymbol{f}, \boldsymbol{\varphi}_{i,k,p} \rangle|^2 \tag{7}$$

where each element in vector $\boldsymbol{f}$ denotes the biomarker score of each node in the brain network. The intuition behind $\hat{h}_{i,k,p}$ essentially characterizes the harmonic energy of spreading the neuropathological burden $\boldsymbol{f}$ through pth harmonic wavelet $\boldsymbol{\varphi}_{i,k,p}$ in kth hierarchical module at underlying hub node v_i. In Section 3.2, we will show the enhanced performance of our proposed new neuroimaging biomarkers in classifying CN, EMCI, and LMCI, compared with current state-of-the-art harmonic analysis approaches.

3. Experiments

To evaluate the statistical power of our HAW biomarker, we compare the performance of our proposed harmonic analysis approach to two state-of-the-art harmonic network analysis approaches on both simulated and real neuroimaging data. These two harmonic network analysis approaches include the global common harmonic wave identification method (Chen et al., 2020b) and single-scale harmonic wavelet identification technique (Chen et al., 2021). Thus, we define our proposed region-specific pyramidal multi-scale harmonic wavelets as $\boldsymbol{\Phi}_m$, global common harmonic waves as $\boldsymbol{\Phi}_g$, and single-scale harmonic wavelets as $\boldsymbol{\Phi}_s$. In addition, the empirical biomarkers $\boldsymbol{f}$ is also used as a baseline to compare with our proposed method.

3.1. Evaluation of HAW on simulated data

3.1.1. Data synthesis—In this section, we generate two different groups of simulated biomarker vectors $\left\{\boldsymbol{f}_j^1 \mid j = 1, \ldots, n\right\} \in \mathbb{R}^N$ and $\left\{\boldsymbol{f}_j^2 \mid j = 1, \ldots, n\right\} \in \mathbb{R}^N$ based on a given group-mean adjacency matrix $\bar{\boldsymbol{W}} \in \mathbb{R}^{N \times N}$. Specifically, these two groups of simulated biomarker vectors are generated by the following steps: (1) generating two sets of key nodes and their corresponding propagation patterns based on the nodal degree and the nearest neighbor edges on $\bar{\boldsymbol{W}}$, such as the node 2 with its corresponding hierarchically modular spreading pathways for group 1 (first two rows in Fig. 4(a)), and the node 11 with its corresponding hierarchically modular propagation patterns for group 2 (last two rows in Fig. 4(a)); (2) linearly combining the propagation patterns generated in step 1 with random weights to form two groups of simulated biomarker vectors; (3) adding the Gaussian noise contamination with standard deviation σ into the generated simulated dataset.

3.1.2. Representation capability of region-specific pyramidal multi-scale harmonic wavelets—Here, we use a toy example to illustrate the representation ability of region-specific pyramidal multi-scale harmonic wavelets identified by our proposed method. First, we generate two groups of simulated biomarker vectors with dimension $N = 10$, where the ground truth of key nodes and their corresponding propagation patterns are shown in Fig. 4(a). Secondly, we separately apply l_1-SVM to classify these two groups based on the harmonic-based features generated by our proposed region-specific pyramidal multi-scale harmonic wavelets $\boldsymbol{\Phi}_m$, single-scale harmonic wavelets $\boldsymbol{\Phi}_s$, and global common harmonic waves $\boldsymbol{\Phi}_g$. The top 4 harmonics with the highest weight coefficient in $\boldsymbol{\Phi}_m$, $\boldsymbol{\Phi}_s$, and $\boldsymbol{\Phi}_g$ are respectively selected as the candidate propagation patterns, as shown in Fig. 4(b–d). It is clear that (1) the region-specific pyramidal multi-scale harmonic wavelets identified by our proposed method are closest to the ground truth of propagation patterns, compared to the other two harmonic analysis methods. (2) The single-scale harmonic wavelet identification method can capture the first modular propagation patterns (shown in the first two rows of Fig. 4(c)), but exhibits poor performance in identifying second modular propagation patterns (shown in the last two rows of Fig. 4(c)). (3) Due to the global nature of the global common harmonic waves, such harmonics are hard to characterize the localized propagation patterns, as shown in Fig. 4(d).

3.1.3. Accuracy of classification, underlying hub detection and propagation pattern identification—

In this section, we are interested in evaluating the performance of our proposed method in classifying different groups, detecting underlying hub nodes, and identifying hierarchically modular propagation patterns. We generate two groups of the simulated datasets based on a given graph with $N = 148$ nodes, where each group consists of 15 key hub nodes and each hub node corresponds to three hierarchically modular propagation patterns. The accuracy of classification based on multi-scale wavelets $\boldsymbol{\Phi}_m$, single-scale wavelets $\boldsymbol{\Phi}_s$, global harmonics $\boldsymbol{\Phi}_g$, and original biomarkers $\boldsymbol{f}$ under various Gaussian noise contaminations σ is shown in Fig. 5(a). Since global common harmonic waves have the limitation of global-ness, we apply our proposed method and single-scale harmonic wavelet identification method to calculate the accuracy of detecting underlying hubs and multi-scale propagation patterns, as shown in Fig. 5(b,c). It is apparent that (1) the harmonic network analysis methods ($\boldsymbol{\Phi}_m$, $\boldsymbol{\Phi}_s$, and $\boldsymbol{\Phi}_g$) achieve higher stratification accuracy than original biomarkers $\boldsymbol{f}$. Among them, our proposed method outperforms the single-scale wavelets and global harmonics. (2) Since the harmonic wavelets ($\boldsymbol{\Phi}_m$ and $\boldsymbol{\Phi}_s$) have the power to characterize the localized propagation patterns, they are capable of locating the underlying hub nodes and thus achieve high hub node identification accuracy, while our proposed method is slightly better than the single-scale wavelet identification method. (3) Due to the hierarchically modular property of our proposed wavelets $\boldsymbol{\Phi}_m$, it exhibits an enhanced ability to identify the propagation patterns, compared to the single-scale harmonic wavelets $\boldsymbol{\Phi}_s$.

3.2. Evaluation of HAW on ADNI data

Training Data.—In this section, we collect neuroimaging data of 138 subjects (shown in Table 2), including T1-weighted MR and DWI images from the ADNI database, to construct the structural brain networks for identifying region-specific pyramidal multi-scale harmonic wavelets $\{\boldsymbol{\Phi}_{i,k} \mid i = 1, \ldots, m; k = 1,2,3\}$. Each structural brain network can be constructed by the following major image processing steps. First, we parcellate the cortical surface into 148 cortical regions based on a T1-weighted MR image in the light of a Destrieux atlas (Destrieux et al., 2010). Then, we apply surface seed-based probabilistic fiber tractography (Destrieux et al., 2010) to the DWI image to generate a 148 × 148 anatomical connectivity matrix $\{\boldsymbol{W}_t \mid t = 1, \ldots, 138\}$. **Testing Data.** After learning the region-specific pyramidal multi-scale harmonic wavelets $\{\boldsymbol{\Phi}_{i,k}\}$, we collect another two datasets, including amyloid-PET scanned by AV45 and tau-PET neuroimaging datasets from ADNI for the downstream analyses. The demographic information of testing data is shown in Table 3. Similarly, we adopt the above-mentioned image processing pipeline to parcellate the cortical surface and calculate the standard update value ratio (SUVR) of each brain region for each PET image as an instance of empirical biomarkers $\{\boldsymbol{f}_s \mid s = 1, \ldots, S\}$. The detailed information of neuroimaging data preprocessing can be found in the Supplementary material.

3.2.1. Evaluating the statistical power of HAW biomarker on amyloid-PET data—In what follows, we estimate the statistical power of our HAW biomarker in stratifying the aging subjects in the pre-clinical stage of AD, identifying the underlying AD-related brain regions, discovering the frequency-based harmonic wavelet alterations, and investigating the association between clinical information and significant harmonic wavelets on amyloid-PET neuroimaging data.

First, we build three group comparisons (CN/LMCI, CN/EMCI, and EMCI/LMCI) of amyloid biomarkers. For each comparison, we use the amyloid HAW biomarkers based on our harmonic wavelets $\boldsymbol{\Phi}_m$ to train the classifier using l_1-SVM optimized by the public toolbox LIBLINEAR (Fan et al., 2008). The l_1-SVM applies the least square loss function to conduct the reconstruction error and embeds feature selection by the l_1-norm regularization term on the coefficient matrix. To compare the classification power across harmonic network analysis methods, we separately train l_1 - SVM on harmonic-based features based on global common harmonic waves $\boldsymbol{\Phi}_g$ and single-scale harmonic wavelets $\boldsymbol{\Phi}_s$. To demonstrate the advantage of harmonic-based features over the empirical amyloid biomarkers, we also train l_1-SVM classifier using the amyloid SUVR score $\boldsymbol{f}$. Finally, the classification performance, including accuracy, specificity, sensitivity, and F-score, is evaluated using 10-fold cross-validation. The final results are shown in Table 4. It is easy to draw that (1) our amyloid HAW biomarker achieves the highest accuracy, specificity, sensitivity, and F-score over all other methods in three group comparisons, where the red star '*' indicates that our results are significantly better than those of the compared methods with $p < 0.01$; (2) the classification performance using harmonic wavelets ($\boldsymbol{\Phi}_m$ and $\boldsymbol{\Phi}_s$) is superior to those of global harmonic waves $\boldsymbol{\Phi}_g$, indicating the localized oscillation patterns in the harmonic wavelets are more appropriate for characterizing the propagation patterns of neuropathological burdens than global harmonic waves; (3) all harmonic-based features outperform empirical biomarkers $\boldsymbol{f}$, which indicate the great potential of applying harmonic network analysis approaches in the early diagnosis of AD.

Second, benefiting from the feature selection of l_1-SVM classifier, we show the Manhattan plot of the feature weight matrix obtained using the trained l_1-SVM by taking CN/LMCI group comparison as an example in the first row of Fig. 6, where the panels from left to right represent the weight coefficients of the first, second, and third-scale harmonic wavelets respectively. We use different colors to denote the frequency of the harmonic wavelet. Moreover, we extract the top five key nodes depending on the highest weight coefficient across the spectrum of the amyloid HAW biomarkers from three different scales, respectively. Next, we calculate the betweenness and local efficiency for each node, as shown in the second row of Fig. 6, where the nodes at the first, second, and third scale are tagged in red, green, and blue respectively. The results of the other three centrality measurements (degree, pagerank, and participation coefficient) are shown in Suppl. Fig. S1. It is clear that the betweenness of those key nodes on a large scale is significantly higher than those on a small scale, while the local efficiency is contrary. These results indicate our proposed multi-scale harmonic wavelet analysis approach has the potential not only to discover the significant brain regions with high degree and local efficiency (putative provincial hubs), but also to identify the significant brain regions with high betweenness score (putative connector hubs). Some of these identified nodes have been demonstrated to be closely related to the development and progression of AD, such as posterior cingulate (Buckner et al., 2009) and inferior frontal (Lin et al., 2017).

Third, we explore the frequency-based harmonic wavelet alterations on the amyloid deposition by using the learned region-specific pyramidal multi-scale harmonic wavelets. Recall we have identified in total fifteen significant brain regions from three different scales in CN/LMCI comparison using amyloid HAW biomarkers. Here, we focus on the significant harmonic wavelets associated with these fifteen brain regions (shown in Fig. 7(a)). We first calculate the total energy of significant harmonic wavelets associated with the fifteen identified brain regions for each subject and plot its distribution for CN (in red) and LMCI (in green) groups in Fig. 7(b). These results suggest that the empirical amyloid along the propagation pathway across the brain network raises the harmonic energy of particular harmonic wavelets, which ultimately leads to cognitive decline. Moreover, we visualize the top three significant harmonic wavelets with the highest weight coefficients in different scales in Fig. 7(c), where the red node denotes the central hub node, and the red/blue arrows indicate the positive/negative oscillations in each harmonic wavelet. These harmonic wavelets have great potential in characterizing the spreading pathways of neuropathological burdens related to the development of AD.

Fourth, we are interested in further research on whether there is a significant association between clinical information and the HAW biomarkers of identified significant harmonic wavelets. Here, the general linear model (GLM) is applied to predict the mini-mental state examination (MMSE) score using our HAW biomarkers, where age and gender are added as the confounders to reduce their influence in our statistical model. We apply the top three significant harmonic wavelets in different scales (shown in Fig. 7(c)) for GLM analyses and plot the statistical results in Fig. 8. It is apparent that (1) 100%(9/9) HAW biomarkers manifest a significant association ($p < 0.01$) with the MMSE score on amyloid-PET data. (2) The significant amyloid HAW biomarkers are negatively associated with the MMSE scores, which is in line with the findings above.

3.2.2. Evaluating the statistical power of HAW biomarker on tau-PET data—

Similarly, we also separately train the l_1-SVM classifier on our tau HAW biomarkers, harmonic-based features based on global common harmonic waves $\boldsymbol{\Phi}_g$ and single-scale harmonic wavelets $\boldsymbol{\Phi}_s$, as well as tau SUVR score $\boldsymbol{f}$ to evaluate the classification performance using 10-fold cross-validation. The classification results of CN/EMCI, EMCI/LMCI, and CN/LMCI group comparison, using our HAW biomarker and the other three biomarkers are shown in Table 5, where our tau HAW biomarker significantly outperforms the other three biomarkers on the accuracy, sensitivity, specificity, and F-score scores ($p < 0.01$). Then, we show the Manhattan plot of the weight coefficient matrix for all harmonic wavelets (3 scales × 40 regions × 6 harmonic frequencies) in CN/LMCI group comparison (shown in the first row of Fig. 9). The top five significant brain regions with the highest average weight coefficient (significant harmonic wavelet) for each scale are selected. We calculate the betweenness and local efficiency score for fifteen brain regions, and plot these scores in the second row of Fig. 9. These results manifest similar findings

(67%(10/15) key node coincidence rate) of Fig. 6 on amyloid-PET data, indicating the efficiency of our proposed method in identifying the putative hub nodes relevant to the development of AD. Furthermore, since fifteen brain regions (shown in Fig. 10(a)) have been identified as showing significant CN/LMCI group differences, we calculate the total energy of significant harmonic wavelets associated with these fifteen identified brain regions for each subject and plot their distribution for CN (in red) and LMCI (in green) groups in Fig. 10(b). The histogram of whole-brain harmonic energy illustrates a similar trend as the amyloid HAW biomarkers that the higher aggregation of tau tangles in the late-stage aging cohort produces a higher harmonic energy load in the brain network system. The top three significant harmonic wavelets for each scale mapped on the cortical surface are also shown in Fig. 10(c) respectively. We also apply the GLM model to the top three significant tau HAW biomarkers for each scale to predict the MMSE score and plot their statistical results in Fig. 11, where 78%(7/9) tau HAW biomarkers show a significantly negative association with the MMSE score.

4. Conclusion

In this paper, we propose a proof-of-concept harmonic wavelet analysis approach to identify the AD-related brain regions that are actively involved in the spreading pathways of neuropathological events. The backbone of our proposed method is a set of region-specific pyramidal multi-scale harmonic wavelets that allow us to characterize the propagation patterns of neuropathological burdens from multiple hierarchical modules centered at particular brain regions. In light of this, we present a manifold-based optimization method to generate harmonic wavelets by integrating the intrinsic characteristics of the brain-network organization, such as hub nodes and hierarchical modularity. Compared with other harmonic analysis methods, our proposed method achieves enhanced statistical power in group comparison on both simulated and ADNI neuroimaging datasets. In the future, we plan to investigate the association between the region-specific pyramidal multi-scale harmonic wavelets and genetic factors in AD progression.

Supplementary Material

Refer to Web version on PubMed Central for supplementary material.

Acknowledgments

This work was supported in part by the National Key Research and Development Program of China (2022YFE0112200), the Key-Area Research and Development of Guangdong Province (2022A0505050014, 2020B1111190001), the Key-Area Research and Development Program of Guangzhou City (202206030009), the National Natural Science Foundation of China (U21A20520, 62172112, 62102153), the Natural Science Foundation of Guangdong Province of China (2022A1515011162), the China Postdoctoral Science Foundation (2021M691062), and in part by the Alzheimer’s Disease Neuroimaging Initiative (ADNI).

Data availability

Data will be made available on request.

References

Araque Caballero MÁ, Suárez-Calvet M, Duering M, Franzmeier N, Benzinger T, Fagan AM, Bateman RJ, Jack CR, Levin J, Dichgans M, et al. , 2018. White matter diffusion alterations precede symptom onset in autosomal dominant Alzheimer's disease. Brain 141 (10), 3065–3080. [PubMed: 30239611]

Atasoy S, Donnelly I, Pearson J, 2016. Human brain networks function in connectome-specific harmonic waves. Nature Commun. 7 (1), 1–10.

Atasoy S, Roseman L, Kaelen M, Kringelbach ML, Deco G, Carhart-Harris RL 2017. Connectome-harmonic decomposition of human brain activity reveals dynamical repertoire re-organization under LSD. Sci. Rep. 7 (1), 1–18. [PubMed: 28127051]

Buckner RL, Sepulcre J, Talukdar T, Krienen FM, Liu H, Hedden T, Andrews-Hanna JR, Sperling RA, Johnson KA, 2009. Cortical hubs revealed by intrinsic functional connectivity: mapping, assessment of stability, and relation to Alzheimer's disease. J. Neurosci. 29 (6), 1860–1873. [PubMed: 19211893]

Chen J, Han G, Cai H, Ma J, Kim M, Laurienti P, Wu G, 2020a. Estimating common harmonic waves of brain networks on Stiefel manifold. In: International Conference on Medical Image Computing and Computer-Assisted Intervention. Springer, pp. 367–376.

Chen J, Han G, Cai H, Yang D, Laurienti PJ, Styner M, Wu G, 2020b. Learning common harmonic waves on Stiefel manifold–A new mathematical approach for brain network analyses. IEEE Trans. Med. Imaging 40 (1), 419–430. [PubMed: 33021935]

Chen J, Yang D, Cai H, Styner M, Wu G, 2021. Discovering spreading pathways of neuropathological events in Alzheimer's disease using harmonic wavelets. In: International Conference on Information Processing in Medical Imaging. Springer, pp. 228–240.

Chikuse Y, 2003. Statistics on Special Manifolds, Vol. 174. Springer Science & Business Media.

Conturo TE, Lori NF, Cull TS, Akbudak E, Snyder AZ, Shimony JS, McK-instry RC, Burton H, Raichle ME, 1999. Tracking neuronal fiber pathways in the living human brain. Proc. Natl. Acad. Sci. 96 (18), 10422–10427. [PubMed: 10468624]

Cope TE, Rittman T, Borchert RJ, Jones PS, Vatansever D, Allinson K, Passamonti L, Vazquez Rodriguez P, Bevan-Jones WR, O'Brien JT, et al. , 2018. Tau burden and the functional connectome in Alzheimer's disease and progressive supranuclear palsy. Brain 141 (2), 550–567. [PubMed: 29293892]

Dai Z, Yan C, Li K, Wang Z, Wang J, Cao M, Lin Q, Shu N, Xia M, Bi Y, et al. , 2015. Identifying and mapping connectivity patterns of brain network hubs in Alzheimer's disease. Cerebral Cortex 25 (10), 3723–3742. [PubMed: 25331602]

van Dellen E, Sommer IE, Bohlken MM, Tewarie P, Draaisma L, Zalesky A, Di Biase M, Brown JA, Douw L, Otte WM, et al. , 2018. Minimum spanning tree analysis of the human connectome. Hum. Brain Mapp. 39 (6), 2455–2471. [PubMed: 29468769]

Destrieux C, Fischl B, Dale A, Halgren E, 2010. Automatic parcellation of human cortical gyri and sulci using standard anatomical nomenclature. Neuroimage 53 (1), 1–15. [PubMed: 20547229]

Fan R-E, Chang K-W, Hsieh C-J, Wang X-R, Lin C-J, 2008. LIBLINEAR: A library for large linear classification. J. Mach. Learn. Res. 9, 1871–1874.

Filippi M, Basaia S, Canu E, Imperiale F, Meani A, Caso F, Magnani G, Falautano M, Comi G, Falini A, et al. , 2017. Brain network connectivity differs in early-onset neurodegenerative dementia. Neurology 89 (17), 1764–1772. [PubMed: 28954876]

van den Heuvel MP, Sporns O, 2013. Network hubs in the human brain. Trends in Cognitive Sciences 17 (12), 683–696. [PubMed: 24231140]

Huang S, Zeng W, Shi Y, 2021. Internet-like brain hierarchical network model: Alzheimer's disease study as an example. Comput. Methods Programs Biomed. 211, 106393. [PubMed: 34551380]

Jack CR Jr., Bennett DA, Blennow K, Carrillo MC, Dunn B, Haeberlein SB, Holtzman DM, Jagust W, Jessen F, Karlawish J, et al. , 2018. NIA-AA research framework: toward a biological definition of Alzheimer's disease. Alzheimer's Dement. 14 (4), 535–562. [PubMed: 29653606]

Kruskal JB, 1956. On the shortest spanning subtree of a graph and the traveling salesman problem. Proc. Amer. Math. Soc. 7 (1), 48–50.

Kumar A, Singh A, et al. , 2015. A review on Alzheimer's disease pathophysiology and its management: an update. Pharmacol. Rep. 67 (2), 195–203. [PubMed: 25712639]

Li W, Yang D, Yan C, Chen M, Li Q, Zhu W, Wu G, Alzheimer's Disease Neuroimaging Initiative, et al. , 2022. Characterizing network selectiveness to the dynamic spreading of neuropathological events in Alzheimer's disease. J. Alzheimer's Dis. (Preprint), 1–12.

Lin F, Ren P, Lo RY, Chapman BP, Jacobs A, Baran TM, Porsteinsson AP, Foxe JJ, Initiative ADN, et al. , 2017. Insula and inferior frontal gyrus' activities protect memory performance against Alzheimer's disease pathology in old age. J. Alzheimer's Dis. 55 (2), 669–678. [PubMed: 27716674]

Mattson MP, 2004. Pathways towards and away from Alzheimer's disease. Nature 430 (7000), 631–639. [PubMed: 15295589]

Nie F, Zhang R, Li X, 2017. A generalized power iteration method for solving quadratic problem on the stiefel manifold. Sci. China Inf. Sci. 60 (11), 1–10.

Pievani M, Filippini N, Van Den Heuvel MP, Cappa SF, Frisoni GB, 2014. Brain connectivity in neurodegenerative diseases-from phenotype to proteinopathy. Nat. Rev. Neurol. 10 (11), 620–633. [PubMed: 25287597]

Sepulcre J, Grothe MJ, d'Oleire Uquillas F, Ortiz-Terán L, Diez I, Yang H-S, Jacobs HI, Hanseeuw BJ, Li Q, El-Fakhri G, et al. , 2018. Neurogenetic contributions to amyloid beta and tau spreading in the human cortex. Nat. Med. 24 (12), 1910–1918. [PubMed: 30374196]

Sporns O, Chialvo DR, Kaiser M, Hilgetag CC, 2004. Organization, development and function of complex brain networks. Trends in Cognitive Sciences 8 (9), 418–425. [PubMed: 15350243]

Stam CJ, 2014. Modern network science of neurological disorders. Nat. Rev. Neurosci. 15 (10), 683–695. [PubMed: 25186238]

Vogel JW, Iturria-Medina Y, Strandberg OT, Smith R, Levitis E, Evans AC, Hansson O, 2020. Spread of pathological tau proteins through communicating neurons in human Alzheimer's disease. Nature Commun. 11 (1), 1–15. [PubMed: 31911652]

Wang Y, Yang D, Li Q, Kaufer D, Styner M, Wu G, 2020. Characterizing the propagation pattern of neurodegeneration in Alzheimer's disease by longitudinal network analysis. In: 2020 IEEE 17th International Symposium on Biomedical Imaging (ISBI). IEEE, pp. 292–295.

Wu JW, Hussaini SA, Bastille IM, Rodriguez GA, Mrejeru A, Rilett K, Sanders DW, Cook C, Fu H, Boonen RA, et al. , 2016. Neuronal activity enhances tau propagation and tau pathology in vivo. Nature Neurosci. 19 (8), 1085–1092. [PubMed: 27322420]

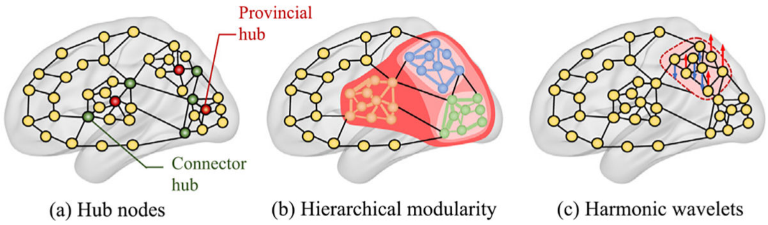

Fig. 1.

(a) The hub nodes in brain network, including provincial hubs (red nodes) and connector hubs (green nodes). (b) The hierarchical modularity of brain network, where modules themselves are modular, thus leading to a nested or fractal topological hierarchy. (c) The harmonic wavelet, where the red/blue arrows indicate the positive/negative oscillations.

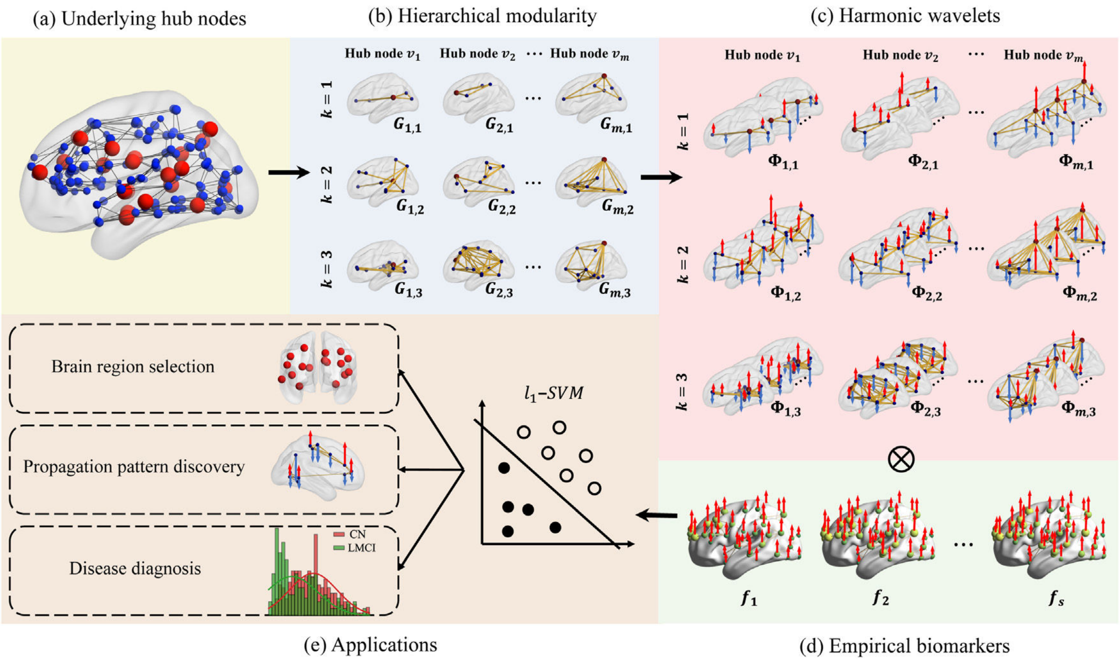

Fig. 2.

Illustration of workflow. (a) The underlying hub nodes v_i (red dots) are estimated by a series of network centrality measurements. (b) The brain network hierarchical module $G_{i,k}$ on kth layer at the underlying hub node v_i is obtained by a hierarchically modular binary mask representation method. (c) The region-specific pyramidal multi-scale harmonic wavelets $\boldsymbol{\Phi}_{i,k}$ located on the hierarchical module $G_{i,k}$ is learned by minimizing our proposed energy function. (d) The empirical biomarkers f_s can be used to combine the learned harmonic wavelets $\boldsymbol{\Phi}_{ik}$ to generate a new neuroimaging biomarker for downstream analyses. (e) The l_1-norm support vector machine (l_1-SVM) is employed to jointly construct feature selection (*i.e.*, AD-related brain regions and propagation patterns) and the classification task (*i.e.,* disease diagnosis).

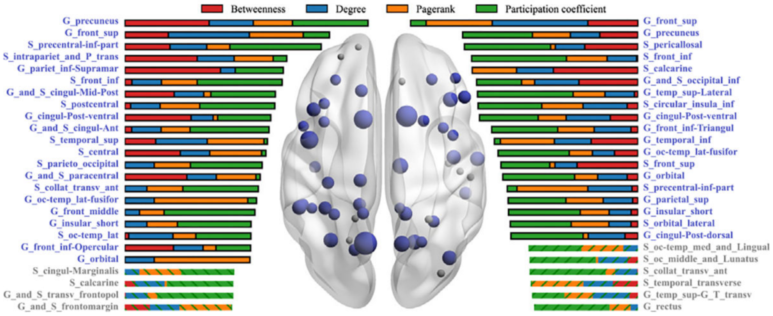

Fig. 3.

Population distribution illustration of betweenness, nodal degree, pagerank, and participation at each node. The top 50 of 148 nodes are shown in order from high to low based on the composite score. The blue nodes in the brain represent the selected underlying hub nodes, whose size stands for the value of composite score. The histogram visualizes the composite score by summing the normalized betweenness (red), nodal degree (blue), pagerank (orange), and participation coefficient (green) for each node.

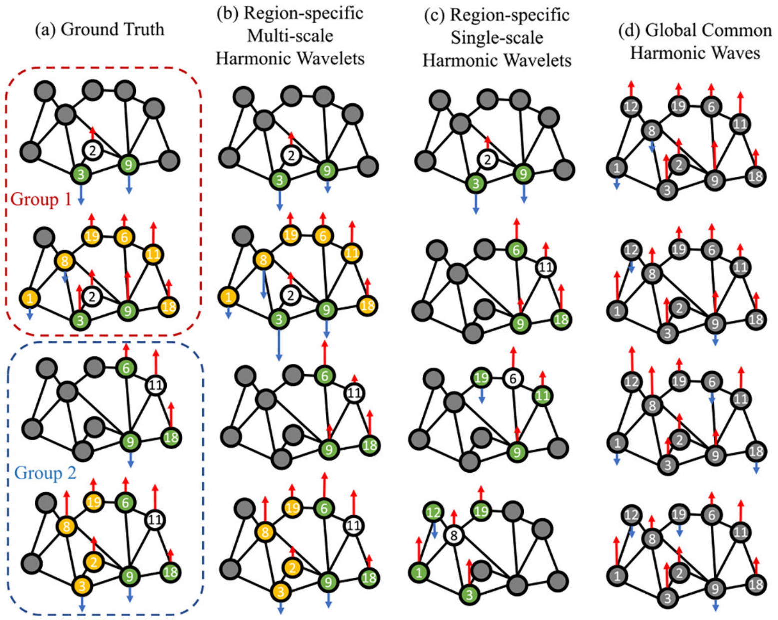

Fig. 4.

Representation power comparison among our multi-scale harmonic wavelets, single-scale harmonic wavelets, and global common harmonic waves. (a) The ground truth of key nodes (v_2 and v_{11}) and their corresponding hierarchically modular propagation patterns, where green nodes represent the first modular nodes and yellow nodes stand for the second modular nodes. (b) the oscillation patterns of the top 4 multi-scale harmonic wavelets detected by our method. (c) in the context of single-scale harmonic wavelets. (d) in the context of global common harmonic waves.

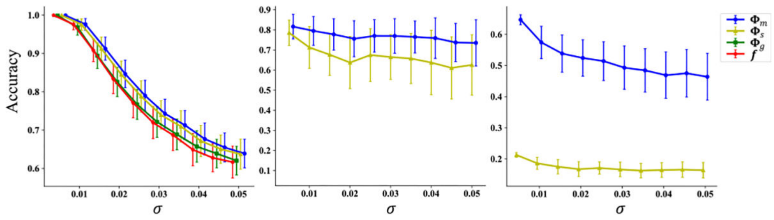

(a) Classification (b) Underlying hub detection (c) Propagation pattern identification

Fig. 5.

A comparison of performance on (a) classification, (b) underlying hub detection, and (c) propagation pattern identification under various noise contaminations. The x-axis and y-axis represent the noise standard deviation σ and accuracy, respectively.

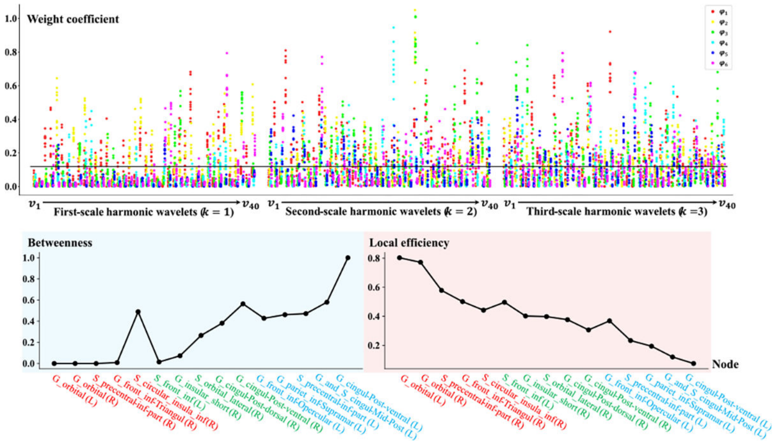

Fig. 6.

Illustration of the significant brain region identification in CN/LMCI comparison using amyloid HAW biomarkers. The first row shows the Manhattan plot of SVM weight coefficients of region-specific pyramidal multi-scale harmonic wavelets. The black line is located at the average of all SVM weight coefficients. The second row visualizes the line plot of betweenness and local efficiency at the top five key nodes from the first (red), second (green), and third (blue) scales. (L) stands for the left hemisphere of the brain, while (R) stands for the right correspondingly.

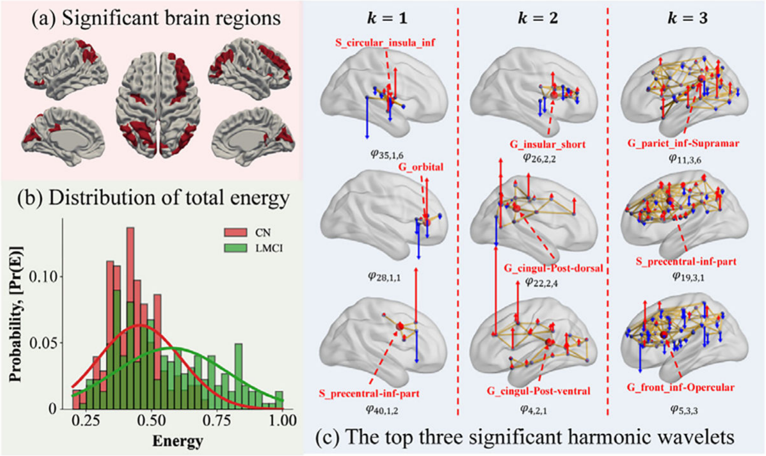

Fig. 7.

Illustration of the frequency-based harmonic wavelet alteration discovery in CN/LMCI comparison using amyloid HAW biomarkers. In (a), we map the fifteen significant brain regions to the cortical surface. In (b), we show the histogram of total energy of the significant harmonic wavelets associated with the fifteen identified brain regions for CN and LMCI groups in red and green, respectively. In (c), we visualize the top three significant harmonic wavelets in different scales, and the red/blue arrows indicate the positive/negative oscillations in each harmonic wavelet.

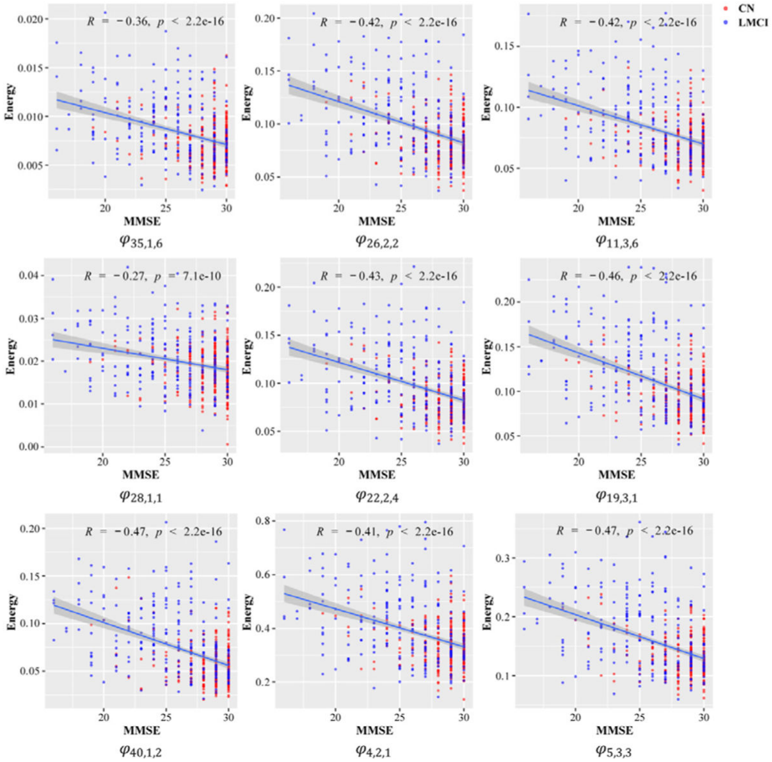

$\varphi_{35,1,6}$ $\varphi_{26,2,2}$ $\varphi_{11,3,6}$

$\varphi_{28,1,1}$ $\varphi_{22,2,4}$ $\varphi_{19,3,1}$

$\varphi_{40,1,2}$ $\varphi_{4,2,1}$ $\varphi_{5,3,3}$

Fig. 8.

The association analyses between significant HAW biomarkers and clinical information (MMSE) on amyloid-PET data. The subjects in CN and LMCI group are represented in red and blue dot, respectively. In addition, the statistical results (R value and p value) are also provided in each panel.

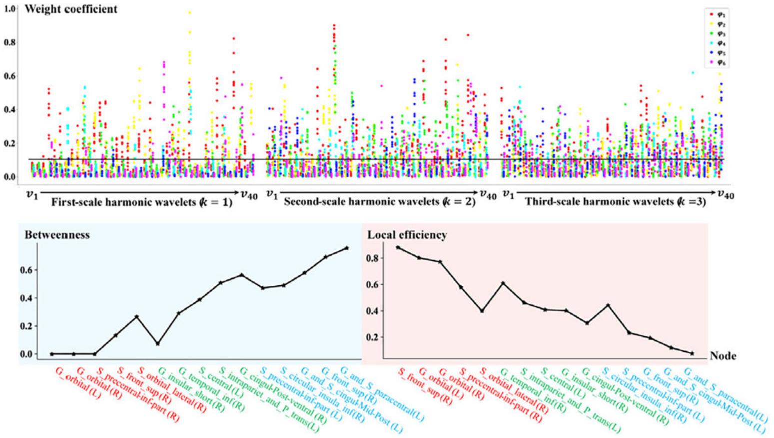

Fig. 9.

Illustration of significant brain region identification in CN/LMCI comparison using tau HAW biomarkers. The symbols and meanings in Fig. 6 also apply to those in this figure. Please refer to the captions of Fig. 6.

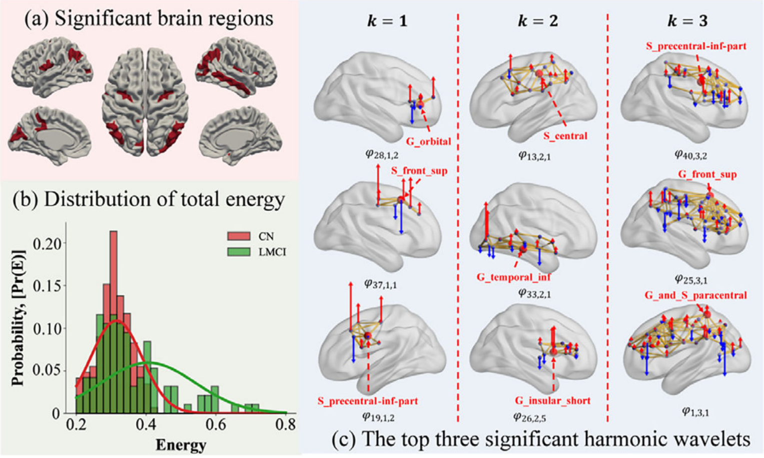

Fig. 10.

Illustration of the frequency-based harmonic wavelet alteration discovery in CN/LMCI comparison using tau HAW biomarkers. The symbols and meanings in (a)–(c) of Fig. 7 also apply to (a)–(c) in this figure, respectively. Please refer to the captions of Fig. 7.

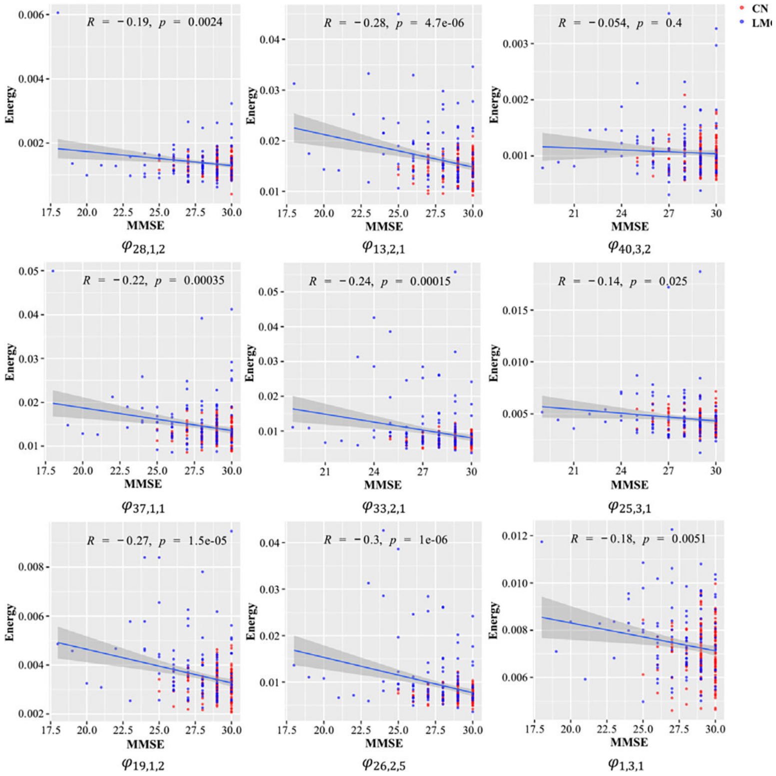

$\varphi_{28,1,2}$ $\varphi_{13,2,1}$ $\varphi_{40,3,2}$

$\varphi_{37,1,1}$ $\varphi_{33,2,1}$ $\varphi_{25,3,1}$

$\varphi_{19,1,2}$ $\varphi_{26,2,5}$ $\varphi_{1,3,1}$

Fig. 11.

The association analyses between significant HAW biomarkers and clinical indicator (MMSE) on tau-PET data. The symbols and meanings in Fig. 8 also apply to those in this figure. Please refer to the captions of Fig. 8.

Table 1

List of notations used in this paper.

Notation	Remark
$x, \boldsymbol{x}, \boldsymbol{X}$	Scalar, vector and matrix
$\boldsymbol{W}$	Weighted adjacency matrix
$\widetilde{\boldsymbol{W}}$	The minimum spanning tree (MST) of weighted adjacency matrix $\boldsymbol{W}$
$\bar{\boldsymbol{W}}$	The average of all $\left\{\widetilde{\boldsymbol{W}}_t \mid t = 1, \ldots, T\right\}$
$\bar{\boldsymbol{L}}$	Graph Laplacian matrix of the group-mean adjacency matrix $\bar{\boldsymbol{W}}$
$\boldsymbol{\Psi}$	Global common harmonic waves
$\boldsymbol{\Phi}_{i,k}$	Harmonic wavelets kth scale at underlying hub node υ_i
$\boldsymbol{\Omega}_i$	The harmonic wavelets on all scales at underlying hub node υ_i
$\boldsymbol{u}_{i,k}$	Hierarchically modular mask on kth layer at underlying hub node υ_i
$\mathbb{R}^N$	N-dimensional real space

Table 2

Demographic information of MRI Neuroimaging Data.

Gender	Number	Range of age	Average age	CN	SMC	EMCI	LMCI	AD
Male	77	55.0~90.3	74.4	15	6	29	12	15
Female	61	55.6~87.8	72.8	14	14	14	9	10
Total	**138**	**55.0~90.3**	**73.7**	**29**	**20**	**43**	**21**	**25**

Table 3

Demographic Information of Amyloid-PET and Tau-PET Neuroimaging Data.

PET	Gender	Number	Range of age	Average age	CN	EMCI	LMCI
Amyloid	Male	450	55.0~91.4	73.4	136	184	130
	Female	389	55.0~89.6	71.7	148	145	96
	Total	**839**	**55.0~91.4**	**72.6**	**284**	**329**	**226**
Tau	Male	180	55.0~90.1	72.2	76	69	35
	Female	150	55.0~88.1	70.1	81	44	25
	Total	**330**	**55.0~90.1**	**71.3**	**157**	**113**	**60**

Table 4

CN/EMCI/LMCI classification results on amyloid-PET data.

Data	Methods	Accuracy	Sensitivity	Specificity	F-score
CN/LMCI	Multi-scale harmonic wavelets $\boldsymbol{\Phi}_m$	**0.738 ± 0.017**	**0.583 ± 0.022**	**0.856 ± 0.020**	**0.658 ± 0.020**
	Single-scale harmonic wavelets $\boldsymbol{\Phi}_s$	0.714 ± 0.016*	0.561 ± 0.018	0.830 ± 0.019*	0.632 ± 0.017
	Global harmonic waves $\boldsymbol{\Phi}_g$	0.700 ± 0.017*	0.550 ± 0.021*	0.821 ± 0.020*	0.613 ± 0.020*
	Empirical amyloid SUVR $\boldsymbol{f}$	0.687 ± 0.018*	0.540 ± 0.022*	0.806 ± 0.020*	0.600 ± 0.021*
CN/EMCI	Multi-scale harmonic wavelets $\boldsymbol{\Phi}_m$	**0.640 ± 0.021**	**0.675 ± 0.023**	**0.615 ± 0.026**	**0.665 ± 0.020**
	Single-scale harmonic wavelets $\boldsymbol{\Phi}_s$	0.607 ± 0.020*	0.634 ± 0.024*	0.583 ± 0.025*	0.630 ± 0.021*
	Global harmonic waves $\boldsymbol{\Phi}_g$	0.596 ± 0.020*	0.628 ± 0.024*	0.567 ± 0.024*	0.623 ± 0.020*
	Empirical amyloid SUVR $\boldsymbol{f}$	0.586 ± 0.020*	0.610 ± 0.024*	0.536 ± 0.025*	0.610 ± 0.020*
EMCI/LMCI	Multi-scale harmonic wavelets $\boldsymbol{\Phi}_m$	**0.665 ± 0.018**	**0.460 ± 0.024**	**0.807 ± 0.019**	**0.515 ± 0.022**
	Single-scale harmonic wavelets $\boldsymbol{\Phi}_s$	0.637 ± 0.018*	0.432 ± 0.026*	0.780 ± 0.019*	0.478 ± 0.024*
	Global harmonic waves $\boldsymbol{\Phi}_g$	0.628 ± 0.020*	0.427 ± 0.025*	0.768 ± 0.020*	0.458 ± 0.026*
	Empirical amyloid SUVR $\boldsymbol{f}$	0.619 ± 0.019*	0.401 ± 0.025*	0.756 ± 0.020*	0.449 ± 0.025*

Table 5

CN/EMCI/LMCI classification results on tau-PET data.

Data	**Wavelets**	**Accuracy**	**Sensitivity**	**Specificity**	**F-score**
CN/LMCI	Multi-scale harmonic wavelets $\boldsymbol{\Phi}_m$	**0.681 ± 0.023**	**0.727 ± 0.026**	**0.650 ± 0.021**	**0.644 ± 0.028**
	Single-scale harmonic wavelets $\boldsymbol{\Phi}_s$	0.662 ± 0.018*	0.700 ± 0.024*	0.636 ± 0.015*	0.625 ± 0.020*
	Global harmonic waves $\boldsymbol{\Phi}_g$	0.651 ± 0.022*	0.692 ± 0.024*	0.623 ± 0.020*	0.614 ± 0.027*
	Empirical tau SUVR $\boldsymbol{f}$	0.636 ± 0.023*	0.678 ± 0.030*	0.614 ± 0.023*	0.608 ± 0.027*
CN/EMCI	Multi-scale harmonic wavelets $\boldsymbol{\Phi}_m$	**0.574 ± 0.027**	**0.577 ± 0.027**	**0.572 ± 0.029**	**0.564 ± 0.039**
	Single-scale harmonic wavelets $\boldsymbol{\Phi}_s$	0.546 ± 0.028*	0.548 ± 0.029*	0.545 ± 0.029*	0.540 ± 0.035*
	Global harmonic waves $\boldsymbol{\Phi}_g$	0.535 ± 0.028*	0.536 ± 0.027*	0.535 ± 0.030*	0.529 ± 0.044*
	Empirical tau SUVR $\boldsymbol{f}$	0.515 ± 0.025*	0.516 ± 0.026*	0.516 ± 0.027*	0.512 ± 0.038*
EMCI/LMCI	Multi-scale harmonic wavelets $\boldsymbol{\Phi}_m$	**0.638 ± 0.020**	**0.625 ± 0.020**	**0.654 ± 0.025**	**0.618 ± 0.025**
	Single-scale harmonic wavelets $\boldsymbol{\Phi}_s$	0.621 ± 0.025*	0.614 ± 0.024*	0.630 ± 0.028*	0.608 ± 0.028*
	Global harmonic waves $\boldsymbol{\Phi}_g$	0.610 ± 0.021*	0.599 ± 0.020*	0.623 ± 0.026*	0.588 ± 0.030*
	Empirical tau SUVR $\boldsymbol{f}$	0.601 ± 0.026*	0.591 ± 0.024*	0.612 ± 0.029*	0.580 ± 0.024*